

602912  
P.8

NASA Technical Memorandum 4203

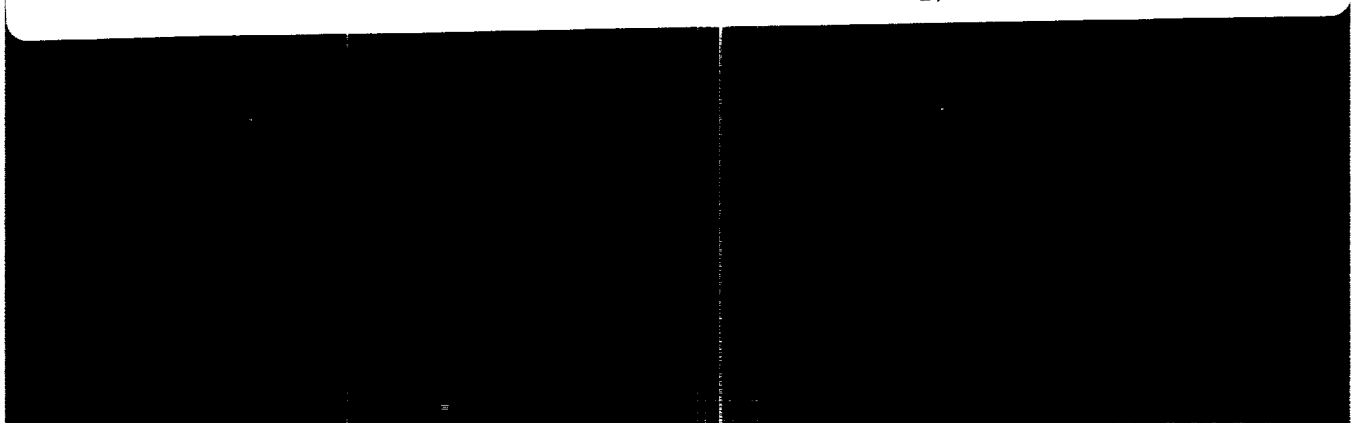
# Collision Forces for Compliant Projectiles

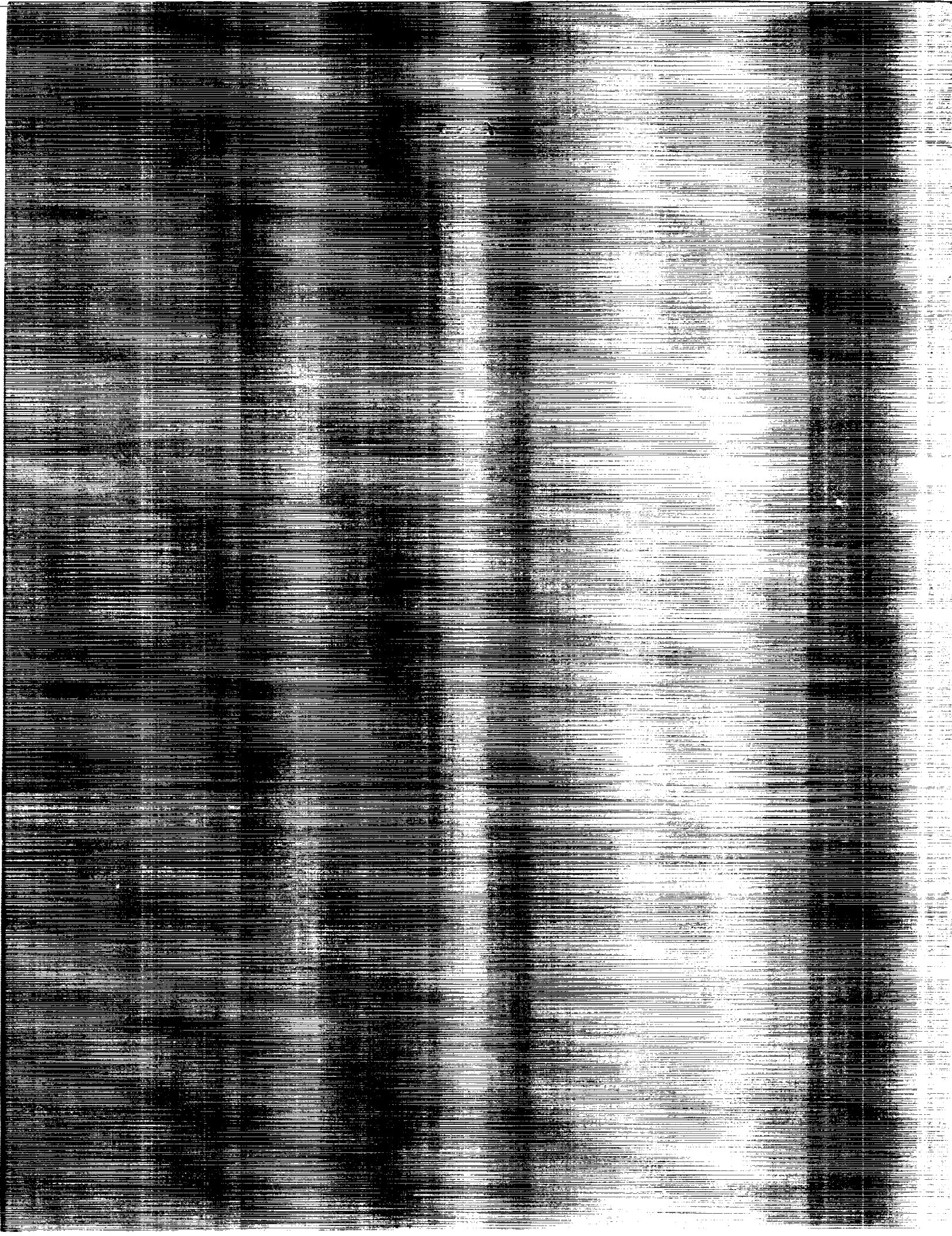
Joseph E. Grady

AUGUST 1990

COMPLIANT PROJECTILES (AJA) 12, COL 20K

Unclas  
H1/59 0302687





NASA Technical Memorandum 4203

# Collision Forces for Compliant Projectiles

Joseph E. Grady  
*Lewis Research Center*  
*Cleveland, Ohio*



National Aeronautics and  
Space Administration  
Office of Management  
Scientific and Technical  
Information Division

1990



# Collision Forces for Compliant Projectiles

Joseph E. Grady  
National Aeronautics and Space Administration  
Lewis Research Center  
Cleveland, Ohio 44135

## Summary

Force histories resulting from the impact of compliant projectiles were determined experimentally. A long instrumented rod was used as the target, and the impact force was calculated directly from the measured strain response. Results from a series of tests on several different sized impactors were used to define four dimensionless parameters that determine, for a specified impactor velocity and size, the amplitude, duration, shape, and impulse of the impact force history.

## Introduction

Impact loading is generally categorized as being in either the low-, medium-, or high-velocity regime. The distinction between the different velocity regimes is most aptly made not in terms of absolute velocities, but rather in terms of the type of deformation experienced by the impactor and target during the impact event (ref. 1). Low-velocity impact is characterized primarily by elastic deformation of impactor and target, and by a small amount of highly localized yielding in the material immediately surrounding the point of contact. Classical elastic contact models (refs. 2 to 6) have been applied successfully to a wide variety of low-velocity impact problems, and this field is quite well developed. Similarly, high-velocity impact has been investigated extensively, particularly during the Apollo spacecraft era (refs. 7 to 10), and more recently for munitions and space station shielding applications (refs. 11 to 14).

The least thoroughly investigated impact regime is the mid-range. In this regime, the impact velocity is high enough to cause finite deformation of the impactor and/or target, but not high enough to generate the extreme amounts of heat and the resulting material phase transformations that can occur during high-velocity impacts. Comparatively few methods are available that can predict with sufficient reliability the transient

force that results from an impact loading in the mid-velocity range. This report contributes toward that goal.

The objectives of this work are, first, to describe a simple experimental technique that can be used to characterize the force history resulting from the impact of a highly compliant projectile undergoing large nonlinear elastic deformation during the impact event, and secondly, to use data from a series of these tests as the basis for an empirical force-history model that describes the force resulting from such an impact.

In the first section of this report, a detailed description of the experimental apparatus and procedure is given. The results of a low velocity "calibration test" are compared with finite-element calculations to demonstrate the validity of the approach. Data from a series of impact tests with silicon rubber projectiles are then used to define, for specified impactor velocity and size, four nondimensional parameters that can be used to determine the amplitude, duration, shape, and impulse of the impact force history.

## Symbols

$D$	impactor diameter
$E$	Young's modulus
$F$	contact force
$F_o$	maximum contact force
$I$	impulse
$K$	contact stiffness
$m$	impactor mass
$n$	exponent
$R$	sphere radius
$T$	contact duration
$t$	time
$t_{F_o}$	time at maximum contact force

$V$	impact velocity
$V_o$	reference velocity
$W$	diagonal matrix of weighting factors
$w_i$	curve-fit weighting factor
$x$	vector of abscissa measurements
$y$	vector of ordinate measurements
$\alpha$	relative indentation
$\nu$	Poisson's ratio
$\Pi_1$ - $\Pi_4$	nondimensional parameters
$\pi$	3.14
$\rho$	mass density

Superscripts:

$\alpha, \beta, \gamma, \delta$  exponents

## Apparatus and Procedure

Longitudinal stress waves propagate nondispersively in a uniform thin bar. An instrumented bar is therefore well suited to determining the force history due to longitudinal impact (refs. 5 and 15).

The experimental apparatus is shown in figure 1. The target was a uniform aluminum 6061-T6 bar 91 cm in length, with a 1.27-cm-diam circular cross section. Two electrical resistance foil strain gages (type EA-13-062AQ-350) were mounted in series at diametrically opposing points at the

midpoint of the bar. This gage arrangement was chosen so as to eliminate the effect of any small flexural waves that would be generated by a slightly eccentric longitudinal impact. The bar was suspended with lightweight 24-gage wire at two support points located at 30 and 60 cm from either end. This arrangement allowed the bar to swing freely in the longitudinal direction after the impact occurred, and resulted in a true free-free boundary condition for the bar. A 2.54-cm-diam aluminum end cap was installed on the proximal end of the bar, as shown in figure 2. The purpose of the end cap was to transfer the compressive force from the compliant impactor to the bar as the impactor deformed and flattened out to a greater diameter than that of the bar.

The impactors were fired at the bar from an air gun. The impact velocity was determined from the measured transit time between two photoelectric diodes which were placed 25 and 50 cm from the exit end of the gun. This sensor arrangement may slightly underestimate the actual velocity of the projectile when it impacts the target. Silicon rubber balls of two different diameters were used as the impactors. Mechanical properties of the impactors are given in reference 16 and summarized in table I. As the compressive strain pulse generated by the longitudinal impact passed the strain gages, the change in voltage output was amplified by the preamplifier (shown in fig. 1), temporarily stored in the waveform recorder, and displayed on the oscilloscope. Permanent copies of the recorded signal were made on the plotter, and manually digitized records of the data were then stored in a computer for later analysis and plotting.

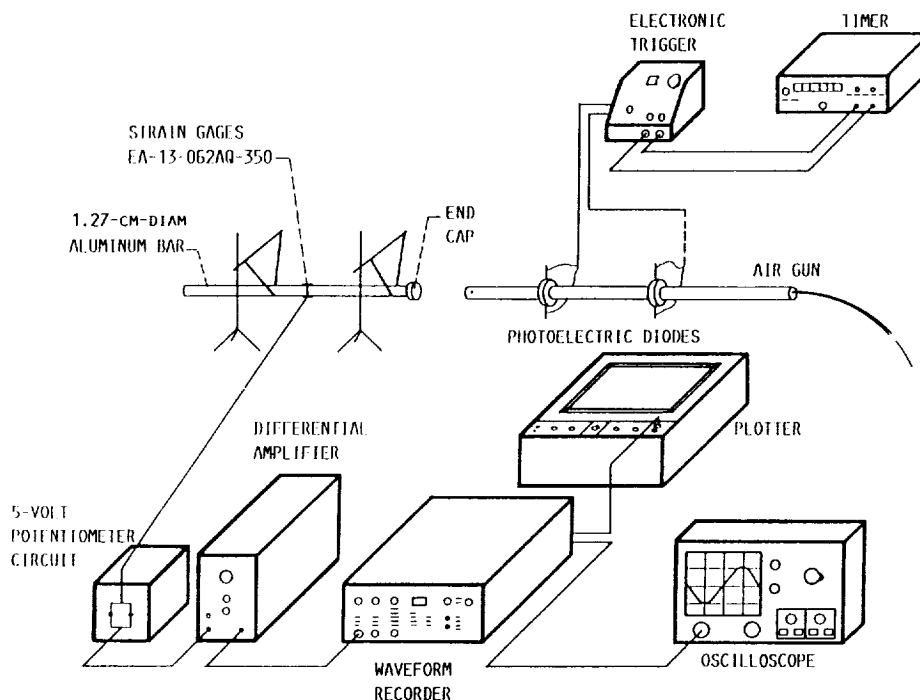


Figure 1.—Longitudinal bar experimental setup.

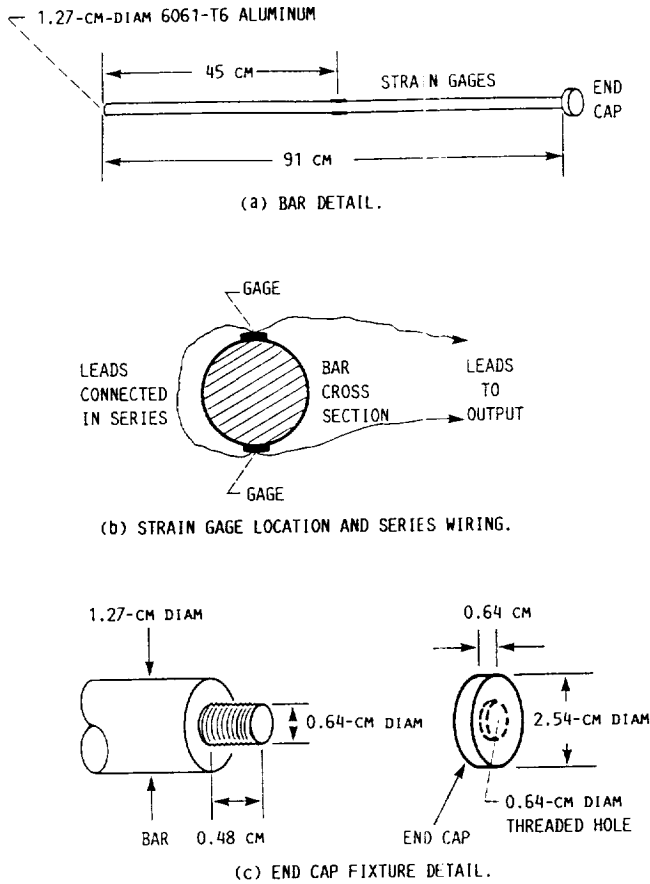


Figure 2.—Bar instrumentation and fixturing.

TABLE I.—MECHANICAL PROPERTIES OF SILICON RUBBER IMPACTORS

[From ref. 16.]

Density, gm/cc	1.03
Hardness, Shore A	65 ± 5
Tensile strength, MPa	5.2
Maximum elongation, %	110

### Calibration Test: Hertzian Impact

Before proceeding to the complicated problem of the high-speed impact of the compliant projectiles, a simpler case was considered. In order to validate the experimental method, a preliminary test and corresponding analysis of the impact of a steel ball on the aluminum bar were performed. During a low-speed impact, the deformation should be mostly elastic, and thus the contact behavior between the steel and aluminum should be well described by the Hertz model, which is summarized briefly here.

Hertz derived the force-indentation relation to describe the elastic contact behavior between two spherical bodies. Hertz's contact law (refs. 2 and 3) is commonly used in both static and dynamic applications to determine the force arising from elastic contact. To briefly summarize Hertz's contact law, we

have

$$F = K\alpha^n \quad (1)$$

where

$F$  = contact force between spheres

$\alpha$  = relative indentation between spheres ( $u_1 - u_2$ )

$n = 1.5$

and

$$K = \frac{4}{3} \sqrt{\frac{R_1 R_2}{R_1 + R_2}} \left( \frac{k_1 k_2}{k_1 + k_2} \right) \quad (2)$$

where

$R_i$  = radii of spheres

$$k_i = \frac{E_i}{1 - \nu_i^2}$$

and  $E_i, \nu_i$  are the respective elastic constants. A special case of interest here occurs when the target is flat ( $R_2 = \infty$ ) in which case equation (2) simplifies to

$$K = \frac{4}{3} \sqrt{R_1} \left( \frac{k_1 k_2}{k_1 + k_2} \right) \quad (3)$$

Figure 3 shows the strain history measured at a single gage location on the bar during a low-speed, elastic impact, at 1.6 m/s. The incident compressive pulse ( $100 < t < 150 \mu s$ ) generated by the impact reflects from the free end of the bar as a tensile pulse ( $275 < t < 325 \mu s$ ) and propagates back to the strain gage. For comparison, a finite-element impact analysis of this calibration test was performed. The bar was modeled with a series of four-degree-of-freedom rod elements (ref. 17) which used the longitudinal displacements ( $u$ ) and the corresponding strains ( $du/dx$ ) at both nodal points as the degrees of freedom. The Hertz contact law (eq. (1)) was incorporated into the finite-element program to define the force-displacement relationship between the impactor and the bar. Newmark's implicit method of direct-time integration (ref. 18) was used to solve the equations of motion for the impactor and the bar simultaneously. The impactor was represented by a lumped mass with an initial velocity toward the bar.

The experimental results in figure 4 compare reasonably well with the finite-element analysis using a 39-element (80-degrees-of-freedom) model of the bar. The contact force history is inferred from this strain measurement by multiplying the strain by the axial stiffness  $EA$  of the aluminum bar and by assuming that the initial pulse travels undistorted (nondispersively) through the bar. The impact force determined in this manner

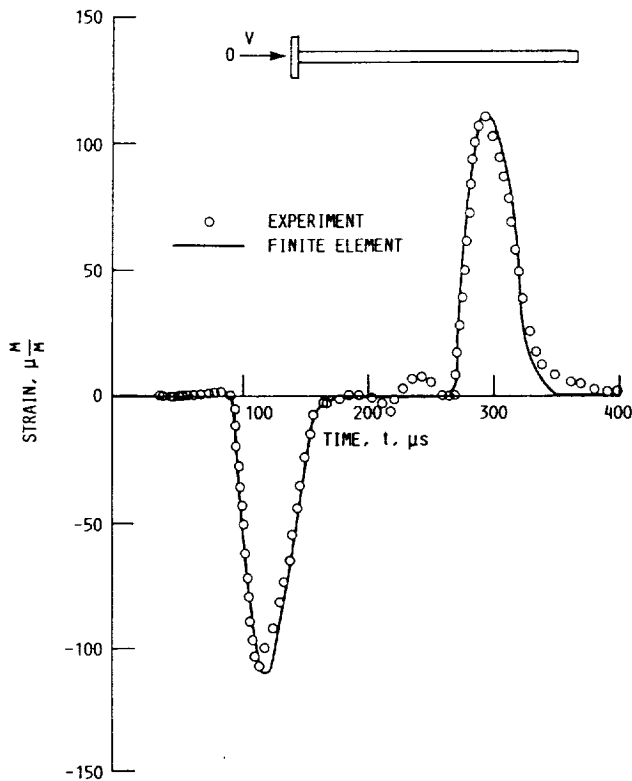


Figure 3.—Strain history at midpoint of bar from 1.6 m/s impact of 1.59-cm-diam steel ball.

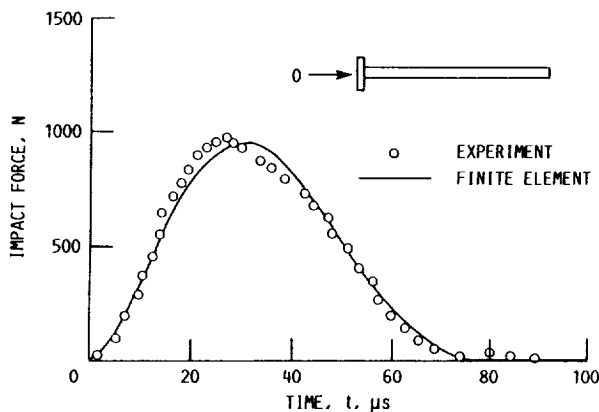


Figure 4.—Force history from 1.6 m/s impact of 1.59-cm-diam steel ball on aluminum bar.

from the strain in figure 3 is compared with that calculated during the finite-element analysis in figure 4. The bar translates longitudinally during contact with the projectile, so the force history is not quite symmetrical about the maximum force, as would be expected if a more rigid target were used. Apparently, the finite-element model accurately calculates the strain history due to a Hertzian impact. In addition, the measured strain response provides a reasonable estimate of the impact force.

### Longitudinal Impact With Soft Projectile

The same bar that was used in the calibration test was then used to measure the strain history resulting from the longitudinal impact of a 1.27-cm-diam silicon rubber ball. The force history will then be calculated from the strain, and from here on will be referred to as the “measured force.”

Figure 5 shows a typical measured impact force versus time behavior for the impact of a 1.27-cm-diam silicon rubber ball. Unlike the more nearly symmetrical Hertzian case, the shape of the curve is noticeably skewed. The force reaches its peak very early in the contact interval and then tapers off slowly before the impactor loses contact with the target. The Hertzian curve in figure 4 could be accurately approximated by a simple half-sine wave of amplitude  $F_0$  and duration  $T$ . The non-Hertzian behavior of the soft impactor, on the other hand, is non-symmetrical; in addition to  $F_0$  and  $T$ , it requires an additional parameter,  $t_{F_0}$  (the time at which the peak force occurs), to characterize its variation with time. Figure 5 identifies the three parameters on the measured curve.

A series of tests was performed to determine how the force history in figure 5 varied with impact velocity. Figures 6 to 8 show the variation in shape and amplitude of the force history resulting from impact of the 1.27-cm-diam balls at velocities ranging from 25 to 150 m/s. Figure 6 shows that the amplitude of the force varies in proportion to  $V^2$ , which is different from the nearly linear variation with velocity predicted by the classical elastic impact models (ref. 4). Figure 7 shows that the contact time varies inversely with the impact velocity, also in contrast to the elastic models, which predict that the two are independent. In plotting these data, the “effective contact time”  $T$  is taken as the duration of the large initial portion of the force history pulse, during which the majority of the impulse is transferred to the target. This approximation is shown in figure 5, and has the effect of ignoring the long trailing “tail” of the force-history curve.

In Figure 8, the time  $t_{F_0}$  at which the maximum impact force occurs is plotted over the velocity range tested. As the impact velocity is increased, the maximum force is reached

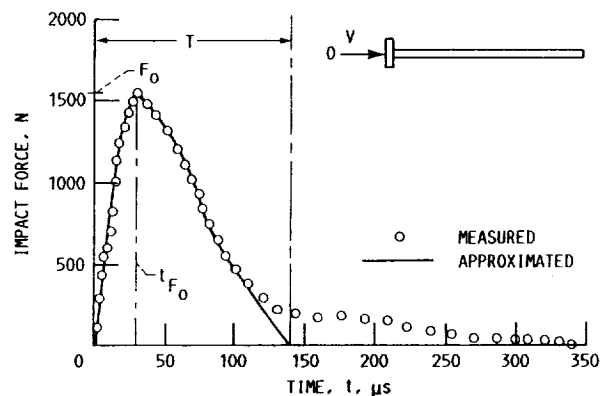


Figure 5.—Force history measured from 88.9 m/s impact of 1.27-cm-diam silicon rubber impactor.

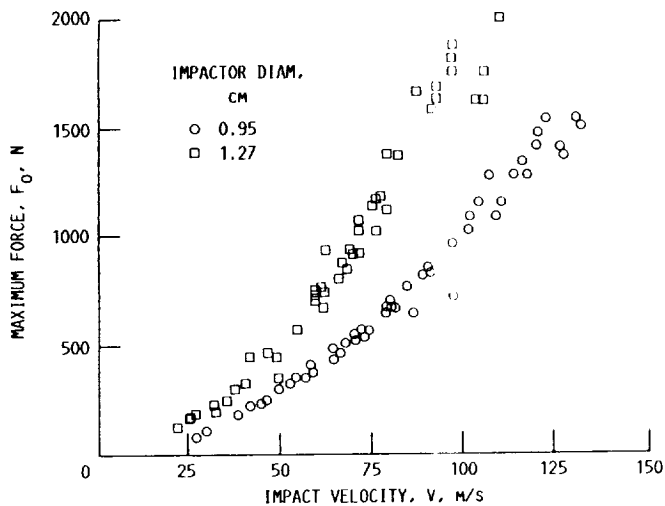


Figure 6.—Variation of amplitude with impact velocity.

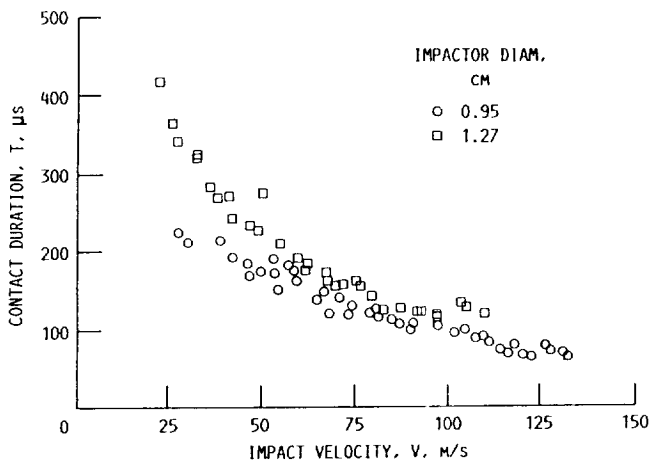


Figure 7.—Variation of contact time with impact velocity.

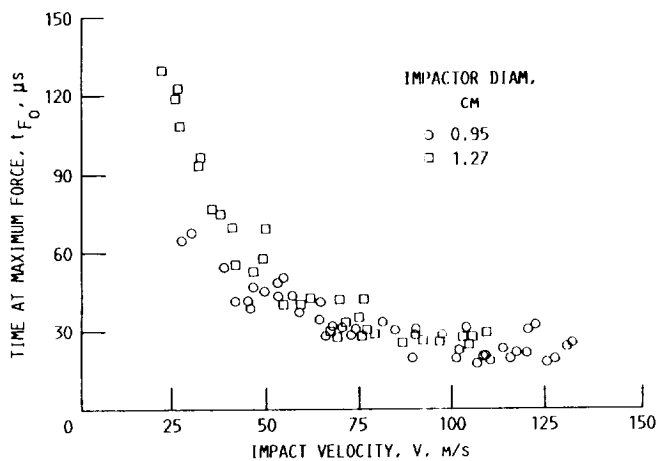


Figure 8.—Time of maximum force.

earlier in the contact interval until it remains approximately constant at velocities above 65 m/s.

The impulse transferred to the target during contact with the impactor is

$$I = \int_0^T F(t) dt \quad (4)$$

where  $F(t)$  is the time history of the impact force and  $T$  is the contact duration. Assuming that the force history in figure 5 can be approximated by two sinusoidal waves as shown, we have

$$F(t) = \begin{cases} F_0 \sin \frac{\pi}{2} \left( \frac{t}{t_{F_0}} \right) & \text{for } 0 < t < t_{F_0} \\ F_0 \cos \frac{\pi}{2} \left( \frac{t - t_{F_0}}{T - t_{F_0}} \right) & \text{for } t_{F_0} < t < T \\ 0 & \text{for } t > T \end{cases} \quad (5)$$

which, after substitution into equation (4), give

$$I = \frac{2}{\pi} F_0 T \quad (6)$$

The impulse calculated by using equation (6) is shown in figure 9 to vary linearly with impact velocity.

A second series of tests was conducted with 0.95-cm-diam impactors of the same silicon rubber material. The analogous results are overlaid on figures 6 to 9 for comparison. The trends observed in the earlier series of tests apparently do not depend on the impactor size, but instead are characteristic of the material. All measured data show the same trends. The

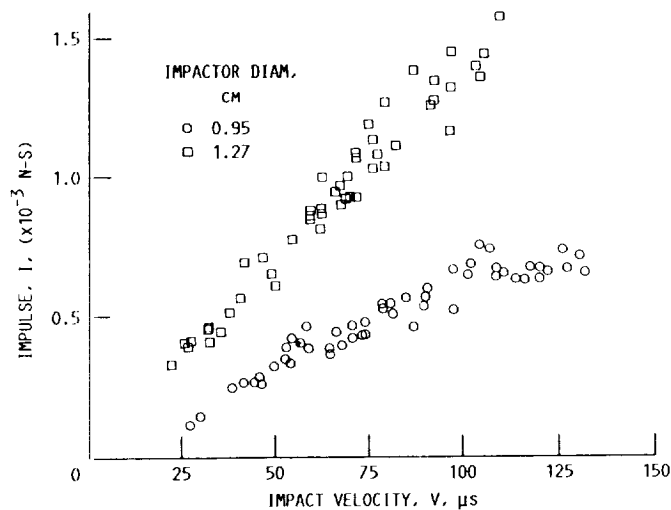


Figure 9.—Measured impulse versus impact velocity.

numerical differences in the measured impact force histories are due to the smaller mass of the second impactor.

### Dimensional Analysis

An empirical model is now developed to describe the observed variation of impact force history with impactor size and velocity. The development and notation follow that of Buckingham's "Pi Theorem" (ref. 19).

Specifically, we wish to describe the data in figure 6, which show the variation of maximum contact force  $F_o$  with impact velocity  $V$  and impactor size,  $D$ . We therefore define a parameter  $\Pi_1$ , as:

$$\Pi_1 = F_o^\alpha \rho^\beta V^\gamma D^\delta \quad (7)$$

where  $\rho$  is the mass density of the impactor, and the exponents are chosen such that  $\Pi_1$  is dimensionless. The exponents are determined by rewriting equation (7) in dimensional form, that is,

$$M^\alpha L^\beta T^{-\alpha} = \left(\frac{ML}{T^2}\right)^\alpha \cdot \left(\frac{M}{L^3}\right)^\beta \cdot \left(\frac{L}{T}\right)^\gamma \cdot (L)^\delta \quad (8)$$

By equating exponents of  $M$  on the left side of equation (8) with those on the right, we have

$$0 = \alpha + \beta \quad (9)$$

and by doing the same for  $L$ , we have

$$0 = \alpha - 3\beta + \gamma + \delta \quad (10)$$

and similarly for  $T$ :

$$0 = 2\alpha - \gamma \quad (11)$$

In solving equations (9) to (11) simultaneously for the four exponents, we may choose  $\alpha = 1$  for convenience, giving

$$[\alpha, \beta, \gamma, \delta] = [1, -1, -2, -2] \quad (12)$$

or, using the definition of  $\Pi_1$  in equation (7), we have

$$\Pi_1 = \frac{F_o}{\rho V^2 D^2} \quad (13)$$

as the dimensionless parameter. The data in figure 6 have therefore been replotted in figure 10 by using the denominator ( $\rho V^2 D^2$ ) in equation (13) as the  $X$  axis. A linear curve-fit is used to calculate the slope of the line that best fits the measured data. The slope  $m$  of the line

$$y = mx \quad (14)$$

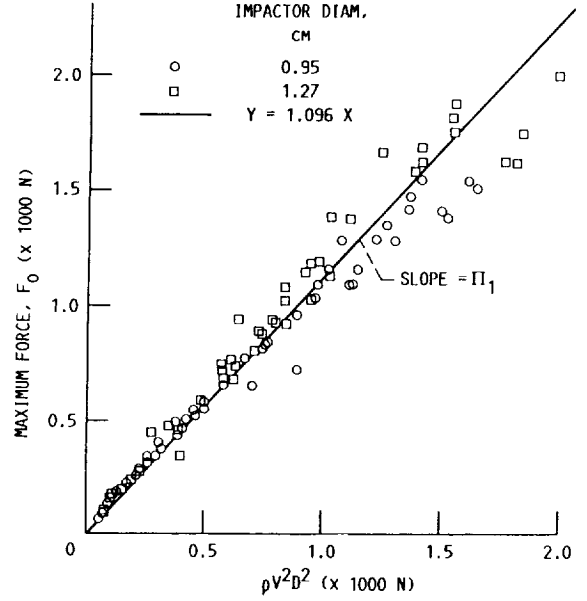


Figure 10.—Least-squares curve-fit for  $\Pi_1$ .

shown in figure 10 is calculated by using a least-squares curve-fit (ref. 20):

$$m = \frac{x^T W y}{x^T W x} \quad (15)$$

where, if  $n$  separate measurements have been taken,  $x$  and  $y$  are  $(n \times 1)$  vectors of the ordinate and abscissa values, respectively, and

$$W = \begin{bmatrix} w_1 & & & & \\ & w_2 & & & \\ & & w_3 & & \\ & & & \ddots & \\ & & & & w_n \end{bmatrix} \quad (16)$$

is an  $(n \times n)$  diagonal matrix of weighting factors. Figure 10 shows that the variability in the measured force increases as the value of  $\rho V^2 D^2$  is increased. The weighting function for the linear curve-fit shown in figure 10 is therefore taken as

$$w_i = \left(\frac{V_o}{V_i}\right)^2 \quad i = 1, n \quad (17)$$

where  $V_i$  is the impact velocity for test "i" and  $V_o$  is a constant reference velocity arbitrarily chosen to make  $w_i$  dimensionless. As a result, the data for the higher impact velocities are weighted less heavily than those at the lower velocities, giving the curve-fit a closer correlation in the low-velocity range, where the linear approximation is more valid.

According to equation (13), the slope of the line in figure 10 can be interpreted as an estimate of  $\Pi_1$ .

The data plotted in figure 7 show the variation of contact time  $T$  with impactor size and velocity. Following the procedure outlined above, we define for this case a second dimensionless parameter  $\Pi_2$ , such that

$$\Pi_2 = T^\alpha \rho^\beta V^\gamma D^\delta \quad (18)$$

where  $T$  has units of time, and the remaining variables have the same definitions as previously. By repeating the process used above to determine the dimensionless form, we have

$$\Pi_2 = \frac{TV}{D} \quad (19)$$

The data in figure 7 are replotted in figure 11 by using the ratio  $D/V$  as the  $X$  axis. The data vary linearly at the higher impact velocities (lower values of  $D/V$ ) so the least-squares weighting function is taken as

$$W_i = \left(\frac{V_i}{V_o}\right)^2 \quad (20)$$

in figure 11. This allows the linear curve-fit to most accurately approximate the data in the region where the linear assumption is most valid. From equation (20), the slope of the line in figure 11 is an estimate of  $\Pi_2$ .

The data plotted in figure 8 show how the time of maximum force,  $t_{F_o}$ , varies with impactor size and velocity. To describe this variable, we define a third dimensionless parameter,  $\Pi_3$ , such that

$$\Pi_3 = t_{F_o}^\alpha \rho^\beta V^\gamma D^\delta \quad (21)$$

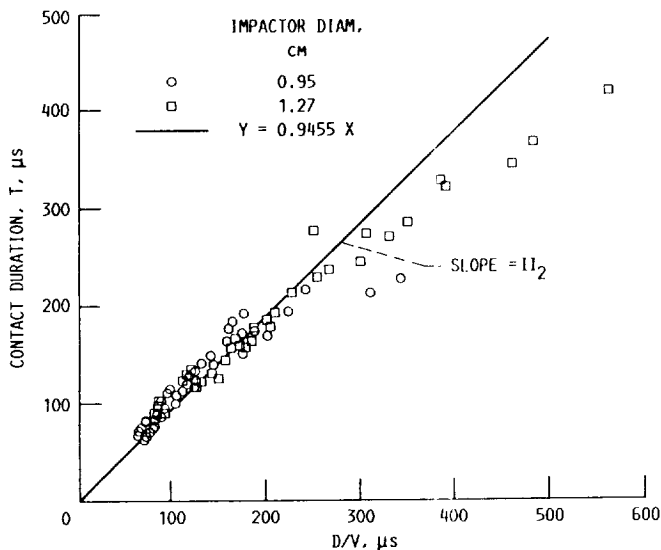


Figure 11.—Least-squares curve-fit for  $\Pi_2$ .

where  $t_{F_o}$  has units of time, and the values of the exponents are to be determined. Repeating the above process for  $\Pi_3$  gives

$$\Pi_3 = \frac{t_{F_o} V}{D} \quad (22)$$

so the data in figure 8 are replotted as a function of  $D/V$  in figure 12. The data vary linearly throughout the range of impact velocities tested, so no weighting is used in the linear curve-fit. The slope of the line in figure 12 is an estimate of  $\Pi_3$  for the given impact conditions.

Finally, a fourth dimensionless constant is used to describe the variation of impulse  $I$  with impactor size and velocity. We define in this case

$$\Pi_4 = I^\alpha \rho^\beta V^\gamma D^\delta \quad (23)$$

where impulse  $I$  has units of  $(ML/T)$  and the exponents are to be determined. The procedure used previously gives

$$\Pi_4 = \frac{I}{\rho V D^3} \quad (24)$$

The impulse data in figure 9 are therefore replotted in figure 13 with the value of  $\rho V D^3$  as the  $X$  axis. The slope of the line is an estimate of the parameter  $\Pi_4$ . Because the impulse is calculated directly from the measured values of  $F_o$  and  $T$  according to equation (6), it follows that  $\Pi_4$  is not independent of the previous three dimensionless parameters.

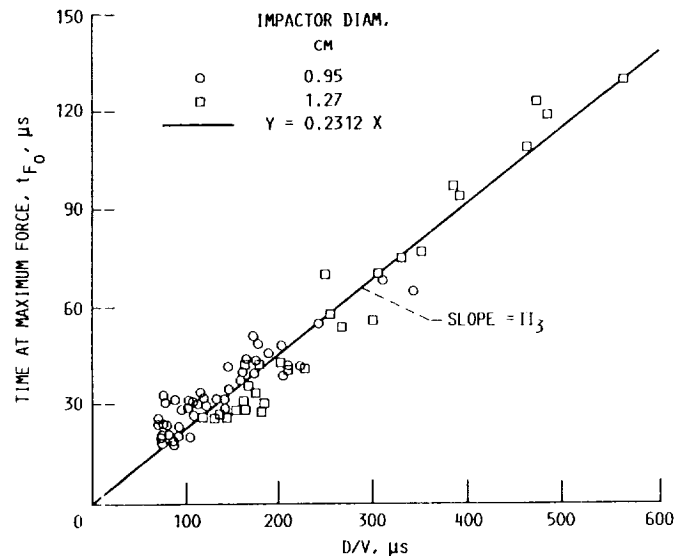


Figure 12.—Least-squares curve-fit for  $\Pi_3$ .

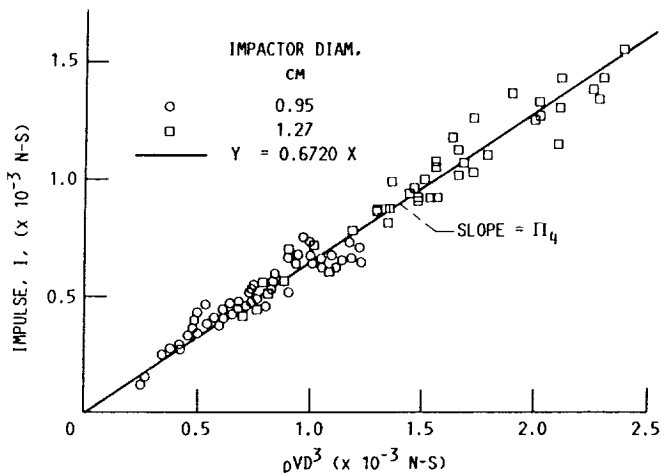


Figure 13.—Least-squares curve-fit for  $\Pi_4$ .

Indeed, the substitution of equations (6) to (8) into equation (10) shows that

$$\Pi_4 = \frac{2\Pi_1\Pi_2}{\pi} \quad (25)$$

as can be verified with the values given in table II.

The measurements of  $F_o$ ,  $T$ ,  $t_{F_o}$  and  $I$ , (shown graphically in figures 6 to 9) are, of course, specific to the particular impactor/target combination used in these tests. Therefore, the values of the four Pi parameters, summarized in table II, will be different from those given here when equations (7) to (10) are applied to different impactor/target combinations. Nonetheless, for impact scenarios involving a large nonlinear elastic deformation of the projectile, the nondimensional modeling approach outlined in the previous section can be used to extrapolate or "scale" the impact force measured from a single test over a range of impactor velocities and sizes.

## Conclusions

A simple experiment to measure the force history resulting from the ballistic impact of a compliant projectile is described.

TABLE II.—DIMENSIONAL ANALYSIS FOR IMPACT FORCE HISTORIES

[Least-squares curve-fit data for figures 10 to 13.]

Parameter	Dimensionless ratio	Empirical value	Weighting factor, $w_i$	Reference figure number
$\Pi_1$	$\frac{F_o}{\rho V^2 D^2}$	1.096	$\left(\frac{V_o}{V_i}\right)^2$	10
$\Pi_2$	$\frac{TV}{D}$	0.946	$\left(\frac{V_i}{V_o}\right)^2$	11
$\Pi_3$	$\frac{t_{F_o} V}{D}$	.231	1.0	12
$\Pi_4$	$\frac{I}{\rho V D^3}$	.672 $\Pi_4$	1.0	13

The results show that for the compliant rubber impactor used here, the velocity dependence of the force history is significantly different from that which would be predicted by classical impact mechanics. This is due primarily to the large nonlinear elastic deformation of the impactor. From the test results, four nondimensional parameters are determined that can now be used to estimate the force history and impulse transferred by a soft impactor to the target for a given set of impact conditions.

Lewis Research Center  
National Aeronautics and Space Administration  
Cleveland, Ohio, June 13, 1990

## References

1. Backman, M.E.; and Goldsmith, W.: The Mechanics of Penetration of Projectiles into Targets. *J. Engr. Sci.*, vol. 16, 1978, pp. 1-99.
2. Hertz, H.: Über die Berührung fester elastischer Körper (The Contact of Elastic Solids). *J. Reine Angew. Math.*, vol. 92, 1882, pp. 156-171.
3. Timoshenko, S.P.; and Goodier, J.N.: *Theory of Elasticity*. 3rd ed., McGraw-Hill, 1970.
4. Goldsmith, W.: *Impact: The Theory and Physical Behaviour of Colliding Solids*. Edward Arnold Publishing, London, 1960.
5. Graff, K.F.: *Wave Motion in Elastic Solids*. Ohio State University Press, 1975, pp. 100-108, 133.
6. Collins, J.A.: *Failure of Materials in Mechanical Design*. John Wiley and Sons, 1981.
7. Proceedings of the Meteoroid Impact and Penetration Workshop. Johnson Manned Spacecraft Center, Clearwater, TX, 1968.
8. Kinslow, R., ed.: *High-Velocity Impact Phenomena*. Academic Press, 1970.
9. Chou, P.C.; and Hopkins, A.K., eds.: *Dynamic Response of Materials to Intense Impulsive Loading*. Air Force Materials Laboratory, Wright Patterson Air Force Base, OH, 1972 (Avail. NTIS, AD-768416).
10. Zukas, J.A., et al.: *Impact Dynamics*. John Wiley and Sons, 1982.
11. Chhabildas, L.C.; and Graham, R.A.: Sudden Impact: Probing Sub-microsecond Shock Waves. *Mech. Eng.*, vol. 110, no. 5, May 1988, pp. 40-51.
12. Swift, H.F.; Bamford, R.; and Chen, R.: Designing Space Vehicle Shields for Meteoroid Protection: A New Analysis. *Advances in Space Research*, vol. 2, no. 12, 1982, pp. 219-234.
13. Coronado, A.R., et al.: Space Station Integrated Wall Design and Penetration Damage Control. NASA CR-179165, 1987.
14. Schonberg, W.P.: Characterizing the Damage Potential of Ricochet Debris Due to an Oblique Hypervelocity Impact. Thirtieth AIAA Structures, Structural Dynamics, and Materials Conference, Vol. 4, AIAA, 1989, pp. 2180-2185.
15. Baker, W.E.; and Dove, R.C.: Measurement of Internal Strains in a Bar Subjected to Longitudinal Impact. *Exper. Mech.*, vol. 2, no. 10, Oct. 1962, pp. 307-311.
16. Clauser, H.P., ed.: *Encyclopedia/Handbook of Materials, Parts, and Finishes*. Technomic Publishing Company, 1976.
17. Yang, T.Y.; and Sun, C.T.: Finite Elements for the Vibration of Framed Shear Walls. *J. Sound Vibr.*, vol. 27, no. 3, Apr. 8, 1973, pp. 297-311.
18. Newmark, N.M.: A Method of Computation for Structural Dynamics. *ASCE J. Eng. Mech. Div.*, vol. 85, no. EM3, July 1959, pp. 67-94.
19. Bridgman, P.W.: *Dimensional Analysis*. Yale University Press, 1943.
20. Noble, B.; and Daniel, J.W.: *Applied Linear Algebra*. 2nd ed., Prentice-Hall, 1977.

1. Report No. NASA TM-4203		2. Government Accession No.		3. Recipient's Catalog No.	
4. Title and Subtitle Collision Forces for Compliant Projectiles				5. Report Date August 1990	
				6. Performing Organization Code	
7. Author(s) Joseph E. Grady				8. Performing Organization Report No. E-5215	
				10. Work Unit No. 505-63-1B	
9. Performing Organization Name and Address National Aeronautics and Space Administration Lewis Research Center Cleveland, Ohio 44135-3191				11. Contract or Grant No.	
				13. Type of Report and Period Covered Technical Memorandum	
12. Sponsoring Agency Name and Address National Aeronautics and Space Administration Washington, D.C. 20546-0001				14. Sponsoring Agency Code	
15. Supplementary Notes					
16. Abstract  Force histories resulting from the impact of compliant projectiles were determined experimentally. A long instrumented rod was used as the target, and the impact force was calculated directly from the measured strain response. Results from a series of tests on several different sized impactors were used to define four dimensionless parameters that determine, for a specified impactor velocity and size, the amplitude, duration, shape, and impulse of the impact force history.					
17. Key Words (Suggested by Author(s)) Impact Structural dynamics Experimental mechanics			18. Distribution Statement Unclassified - Unlimited Subject Category 39		
19. Security Classif. (of this report) Unclassified		20. Security Classif. (of this page) Unclassified		21. No. of pages 13	22. Price* A03

